

Order parameter dynamics in Mn₃Sn driven by DC and pulsed spin-orbit torques

Ankit Shukla, Siyuan Qian, and Shaloo Rakheja

Holonyak Micro and Nanotechnology Laboratory, University of Illinois at Urbana-Champaign, Urbana, IL 61801

(*Electronic mail: ankits4@illinois.edu, siyuanq3@illinois.edu, rakheja@illinois.edu)

(Dated: 30 August 2023)

We numerically investigate and develop analytic models for both the DC and pulsed spin-orbit-torque (SOT)-driven response of order parameter in single-domain Mn₃Sn, which is a metallic antiferromagnet with an anti-chiral 120° spin structure. We show that DC currents above a critical threshold can excite oscillatory dynamics of the order parameter in the gigahertz to terahertz frequency spectrum. Detailed models of the oscillation frequency versus input current are developed and found to be in excellent agreement with the numerical simulations of the dynamics. In the case of pulsed excitation, the magnetization can be switched from one stable state to any of the other five stable states in the Kagome plane by tuning the duration or the amplitude of the current pulse. Precise functional forms of the final switched state versus the input current are derived, offering crucial insights into the switching dynamics of Mn₃Sn. The readout of the magnetic state can be carried out via either the anomalous Hall effect, or the recently demonstrated tunneling magnetoresistance in an all-Mn₃Sn junction. We also discuss possible disturbance of the magnetic order due to heating that may occur if the sample is subject to large currents. Operating the device in pulsed mode or using low DC currents reduces the peak temperature rise in the sample due to Joule heating. Our predictive modeling and simulation results can be used by both theorists and experimentalists to explore the interplay of SOT and the order dynamics in Mn₃Sn, and to further benchmark the device performance.

I. INTRODUCTION

Antiferromagnets (AFMs) are a class of magnetically ordered materials that exhibit negligible net magnetization, owing to the unique arrangement of strongly exchange-coupled spins on the atoms of their unit cells. As a result, AFMs produce negligible stray fields, are robust to external magnetic field perturbations, and their precession frequency, set by the geometric mean of exchange and anisotropy energies, is in the terahertz (THz) regime.¹⁻³ The past decade has witnessed a rapid rise in theoretical and experimental research focused on the fundamental understanding and applications of AFM materials as active spintronic device elements.³⁻⁸ There exists a broad range of AFM materials including insulators, metals, and semiconductors with unique properties that could be exploited to realize magnonic devices,⁹ high-frequency signal generators and detectors,^{5,6,10-15} and non-volatile memory.¹⁶⁻¹⁸ For example, insulators like NiO^{19,20} and MnF₂²¹ are well studied and have the potential to carry charge-less spin waves or magnons. Insulating AFM Cr₂O₃ shows magnetoelectricity below its Néel temperature of 307 K, which was exploited to demonstrate voltage-controlled exchange-bias memory and fully electrically controlled memory devices.²² On the other hand, metallic AFMs have been mostly used as sources of exchange bias in spin valves and tunnel junction-based devices.^{23,24} More recently, there has been significant research activity in non-collinear, chiral metallic AFMs of the form Mn₃X with a triangular spin structure and several intriguing magneto-transport characteristics such as a large spin Hall effect (SHE),²⁵ anomalous Hall effect (AHE),²⁶⁻²⁸ and ferromagnet-like spin-polarized currents.²⁹

Negative chirality materials, such as Mn₃Sn, Mn₃Ge, Mn₃Ga, perhaps best represent the promise of non-collinear metallic AFMs with a potential for ferromagnet-like spin-

tronic devices in which the order parameter could be fully electrically controlled and read-out.³⁰⁻³² In a recent experiment,³³ conducted in a bilayer of heavy metal and Mn₃Sn, a characteristic fluctuation of the Hall resistance was measured in response to a DC current in the heavy metal. This observation could be explained in terms of the rotation of the chiral spin structure of Mn₃Sn driven by spin-orbit torque (SOT). Pal et al. and Krishnaswamy et al. independently showed that Mn₃Sn layers thicker than the spin diffusion length could be switched by seeded SOTs.^{34,35} Here, the SOT sets the spin texture of the AFM in a thin layer at the interface, which acts as the seed for the subsequent setting of the domain configuration of the entire layer. The seeded SOT also requires bringing the temperature of the AFM above its ordering temperature and then cooling it in the presence of the SOT generated in a proximal heavy metal layer. Very recently, tunneling magnetoresistance (TMR) of approximately 2% at room temperature in an all antiferromagnetic tunnel junction consisting of Mn₃Sn/MgO/Mn₃Sn was experimentally measured.³⁶ The TMR in Mn₃Sn originates from the time reversal symmetry breaking and the momentum-dependent spin splitting of bands in the crystal. These recent works highlight the tremendous potential of Mn₃Sn and other negative chirality AFMs to explore and develop spintronic device concepts.

In this paper, we discuss the energy landscape of a thin film of Mn₃Sn in the mono-domain limit and deduce the weak six-fold magnetic anisotropy of the film via perturbation and numerical solutions (Section III). Consequences of the six-fold anisotropy on the equilibrium states, the origin of the weak ferromagnetic moment, and SOT-induced non-equilibrium dynamics are carefully modeled in Sections III and IV. The analytic model of the threshold spin current to drive the system into steady-state oscillations is validated

against numerical simulations of the equation of motion. Because of the weak in-plane magnetic anisotropy, on the order of 100 J/m^3 , we find that the critical spin current to induce dynamic instability of the order parameter in Mn₃Sn could be orders of magnitude lower than that in other AFMs such as NiO^{5,6,12} and Cr₂O₃¹². Additionally, the oscillation frequency of the order parameter in Mn₃Sn could, in principle, be tuned from the gigahertz (GHz) to the terahertz (THz) scale¹⁴. We also examine the response of the system when subject to pulsed spin current. Our results show that by carefully tuning the pulse width of the current (t_{pw}) and the spin charge density injected into the system ($J_s t_{pw}$, where J_s is the spin current density) the evolution of the order parameter across different energy basins, separated by 60° in the phase space, can be controlled. Our results of the SOT-driven dynamics in single-domain Mn₃Sn are closely related to the experimental results of Ref. 33. Previous theoretical works on the current-driven dynamics in collinear as well as non-collinear AFMs have only addressed systems with zero net magnetization and those with two-fold anisotropy.^{14,37,38} Another work focusing on NiO with six-fold anisotropy had only presented numerical aspects of pulsed SOT switching.³⁹ On the other hand, here, we address both the numerical and analytical aspect of current-driven dynamics in six-fold anisotropic system with a small non-zero net magnetization. We also discuss the AHE and TMR detection schemes and present the magnitude of output voltages for typical material parameters in both the cases (Section V). Finally, we highlight the impact of thermal effects on the dynamics of the order parameter and the temperature rise of the sample when DC spin currents are acting on Mn₃Sn to generate high-frequency oscillations (Section VI). Our models highlight the limits, potential, and opportunities of negative chirality metallic AFMs, prominently Mn₃Sn, for developing functional magnetic devices that are fully electrically controlled.

II. CRYSTAL AND SPIN STRUCTURE

Mn₃Sn has a Néel temperature of approximately 420 K and can only be stabilized in excess of Mn atoms. Below this temperature, it crystallizes into a layered hexagonal $D0_{19}$ structure, where the Mn atoms form a Kagome-type lattice in basal planes that are stacked along the c axis ($[0001]$ direction), as shown in Fig. 1(a). In each plane, the Mn atoms are located at the corners of the hexagons whereas the Sn atoms are located at their respective centers. The magnetic moments on the Mn atoms, on the other hand, have been shown by neutron diffraction experiments⁴⁰ to form a noncollinear triangular spin structure with negative chirality, as shown in Fig. 1(b). The nearest neighbor Mn moments (\mathbf{m}_1 , \mathbf{m}_2 and \mathbf{m}_3) are aligned at an angle of approximately 120° , with respect to each other, resulting in a small net magnetic moment \mathbf{m} . The weak ferromagnetism in Mn₃Sn, and similar antiferromagnets such as Mn₃Ge and Mn₃GaN, has been attributed to the geometrical frustration of the triangular antiferromagnetic structure, which leads to slight canting of Mn spins toward in-plane easy axes.⁴¹ The chirality of the spin structure breaks

time reversal symmetry and leads to momentum-dependent Berry curvature and modifies the magneto-transport signals in Mn₃Sn.^{26,41} Switching from one chirality to another flips the sign of the Berry curvature and thus the sign of magneto-transport signals that are odd with respect to Berry curvature.

Previous theoretical works^{42,43} posit the aforementioned crystal structure to a hierarchy of interactions typical for 3d transition metal ions—strong Heisenberg exchange, followed by weaker Dzyaloshinskii-Moriya (DM) interaction, with single-ion anisotropy being the weakest. Their model of the magnetic free energy interaction in a unit cell of bulk Mn₃Sn crystal, based on this hierarchy of interactions, predicts the existence of a small in-plane net magnetization, six-fold anisotropy degeneracy, and the deformation of the magnetic texture by an external magnetic field. The basic spin structure of the free energy model in case of Mn₃Sn comprises two triangles, with three spins each, one on each basal plane.^{42,43} While the free energy model of Ref. 42 explicitly considers an interplane exchange interaction in addition to the intraplane exchange interaction, the free energy model of Ref. 43 considers an effective exchange parameter, which includes both these effects. The latter approach simplifies the system of six spins to that of three spins. Therefore, in our work, we assume a free energy model based on the latter approach viz., a system of three magnetic moments.^{14,44}

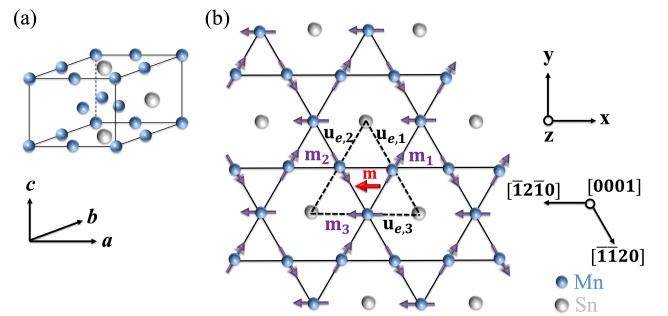


FIG. 1. (a) Layered hexagonal crystal structure of Mn₃Sn. The a and c axes are parallel to the $[\bar{1}2\bar{1}0]$ and $[0001]$ directions, respectively. (b) Hexagonal crystal and inverse triangular spin structure of Mn₃Sn in the basal plane. In each hexagon the Mn atoms are at the corners (blue) while the Sn atoms are at the center (gray). The spins (purple arrows) on neighboring Mn atoms are aligned at an angle of 120° with respect to each other. The dashed lines connecting the Sn atoms represent the three easy axes ($\mathbf{u}_{e,i}$) corresponding to the magnetocrystalline anisotropy. They are ordered counterclockwise whereas \mathbf{m}_1 , \mathbf{m}_2 , and \mathbf{m}_3 are ordered clockwise. The red arrow represents the net magnetization. The z -axis coincides with $[0001]$.

III. FREE ENERGY MODEL AND EQUILIBRIUM STATES

We consider a single domain non-collinear antiferromagnetic particle of Mn₃Sn of size $L_a \times w_a \times d_a$. In the continuum modeling approach, the single domain Mn₃Sn is assumed to be composed of three equivalent interpenetrating sublattices, which are represented by magnetization vectors \mathbf{m}_1 , \mathbf{m}_2 , and \mathbf{m}_3 .^{14,33} Each magnetization vector has a con-

stant saturation magnetization, M_s , and is strongly coupled to the other by a symmetric exchange interaction, characterized by the exchange constant $J_E (> 0)$. In addition, an asymmetric Dzyaloshinskii-Moriya interaction (DMI), characterized by the coefficient $D (> 0)$, and single-ion uniaxial magnetocrystalline anisotropy, characterized by constant $K_e (> 0)$ are assumed to describe the system. The free energy density is, therefore, defined as^{14,44}

$$F(\mathbf{m}_1, \mathbf{m}_2, \mathbf{m}_3) = J_E(\mathbf{m}_1 \cdot \mathbf{m}_2 + \mathbf{m}_2 \cdot \mathbf{m}_3 + \mathbf{m}_3 \cdot \mathbf{m}_1) + D\mathbf{z} \cdot (\mathbf{m}_1 \times \mathbf{m}_2 + \mathbf{m}_2 \times \mathbf{m}_3 + \mathbf{m}_3 \times \mathbf{m}_1) - \sum_{i=1}^3 \left(K_e(\mathbf{m}_i \cdot \mathbf{u}_{e,i})^2 + \mu_0 M_s \mathbf{H}_a \cdot \mathbf{m}_i \right), \quad (1)$$

where $\mathbf{u}_{e,i}$ is the easy axis corresponding to \mathbf{m}_i . Here, they are assumed to be $\mathbf{u}_{e,1} = -(1/2)\mathbf{x} + (\sqrt{3}/2)\mathbf{y}$, $\mathbf{u}_{e,2} = -(1/2)\mathbf{x} - (\sqrt{3}/2)\mathbf{y}$ and $\mathbf{u}_{e,3} = \mathbf{x}$, respectively. Typical value of these energy constants are listed in Table I. The last term in Eq. (1) is the Zeeman energy due to the externally applied magnetic field \mathbf{H}_a . For the results presented in this work no external magnetic field is considered.

Compared to previous works discussing micromagnetic modeling of AFMs,^{14,45} monodomain modeling is applicable for AFM particles that are smaller than the domain size, which is typically 200 – 250 nm for Mn₃Sn.^{33,46} For such length scales spatial variation in exchange and DM interactions can be safely ignored.⁴⁷ The details of the micromagnetic simulation framework, including the boundary conditions, can be consulted from our previous work.¹⁴ Since in this work we focus on the mono-domain limit, the cell dimensions are the same as the physical dimensions of the AFM layer. The thickness of the AFM film plays a role in establishing the spin angular momentum acting on the AFM from the proximal NM. In contrast to the continuum modeling approach presented in this work and in Ref. 33, some previous works have employed a three spin atomistic model.^{34,46,48} Although the atomistic modeling approach is more accurate, it becomes computationally expensive for large systems of size 10's of nm and above since the number of atoms and the associated spins increase. On the other hand, the continuum modeling framework is more suitable for large systems and has been shown to agree well with atomistic simulations in the case of another manganese-based AFM, Mn₂Au.⁴⁹ Therein, the material parameters used in the continuum framework were well calibrated against those in the atomistic model. The material parameters used in our work are also calibrated against an atomistic model as mentioned in Ref. 44

In exchange energy dominant AFMs, such as Mn₃Sn, the hierarchy of energy interactions leads to $J_E \gg D \gg K_e$. As a result, the exchange energy is minimized if the three sublattice vectors are at an angle of $\frac{2\pi}{3}$ with respect to each other. The minimization of the DM interaction energy confines the sublattice vectors to the x-y plane with zero z-component, and enforces a clockwise ordering between the vectors \mathbf{m}_1 , \mathbf{m}_2 , and \mathbf{m}_3 . The magnetocrystalline anisotropy energy would be minimized if each \mathbf{m}_i coincides with its respective $\mathbf{u}_{e,i}$. However, counterclockwise ordering of $\mathbf{u}_{e,1}$, $\mathbf{u}_{e,2}$, and $\mathbf{u}_{e,3}$ along with

the clockwise ordering of \mathbf{m}_1 , \mathbf{m}_2 , and \mathbf{m}_3 implies that all the magnetization vectors cannot coincide with their respective easy axis simultaneously. This would lead to six equilibrium or minimum energy states wherein only of the sublattice vectors is coincident with its easy axis.

TABLE I. List of material parameters for the AFM, Mn₃Sn, and the heavy metal (HM), which is chosen as W, in the SOT device setup.

Parameters	Definition	Values	Ref.
J_E	Exchange constant	$2.4 \times 10^8 \text{ J/m}^3$	44
D	DMI constant	$2 \times 10^7 \text{ J/m}^3$	44
K_e	Uniaxial anisotropy constant	$3 \times 10^6 \text{ J/m}^3$	44
M_s	Saturation magnetization	1.63 T	44
α	Gilbert damping	0.003	48
d_{HM}	Thickness of HM	7 nm	46
ρ_{HM}	Resistivity of HM	$43.8 \mu\Omega \cdot \text{cm}$	46
θ_{SH}	Spin Hall angle for HM	0.06	46

Minimizing Eq. (1) with respect to \mathbf{m}_i leads to six equilibrium states, as shown in Fig. 2. They are given as $\phi_m^{\text{eq}} = n\pi/3$, where $n = \{0, 1, 2, 3, 4, 5\}$. In each case, only one of the three magnetization vectors coincides with its easy axis. A small in-plane average magnetization, $\mathbf{m} = \frac{\mathbf{m}_1 + \mathbf{m}_2 + \mathbf{m}_3}{3}$, is also obtained, depicted by the red arrows in Fig. 2. In each case, \mathbf{m} coincides with the sublattice vector that is aligned along its easy axis. Our numerical calculations reveal the norm of the average magnetization to be equal but very small for all the six ground states, approximately $\|\mathbf{m}\| \approx 3.66 \times 10^{-3}$. Therefore, in Fig. 2, \mathbf{m} is zoomed-in by 100× for the sake of clear presentation. The small non-zero value of $\|\mathbf{m}\|$ suggests that the angle between the sublattice vectors is not exactly 120° , but deviates slightly. Defining this deviation as $\eta_{ij} = \cos^{-1}(\mathbf{m}_i \cdot \mathbf{m}_j) - \frac{2\pi}{3}$, we find that $\eta_{ij} \approx -0.36^\circ$ if either of \mathbf{m}_i or \mathbf{m}_j is coincident with its easy axis while $\eta_{ij} \approx 0.72^\circ$ if neither \mathbf{m}_i nor \mathbf{m}_j coincides with its easy axes. This small canting of sublattice vectors is well known, as mentioned in previous theoretical and experimental works.^{40,41,50} Our numerical results show that $\eta_{12} + \eta_{23} + \eta_{31} = 0$.

To gain further insight into the six-fold degenerate equilibrium states, we adopt a perturbative approach^{42,43,51} to derive a simple model of the energy density. Firstly, the order parameters, viz. sublattice vectors and the average magnetization vector, in the equilibrium states are assumed to be in the x-y plane. Secondly, the angle between \mathbf{m}_i and \mathbf{m}_j is assumed to deviate slightly from 120° . Therefore, we have

$$\mathbf{m} = u_m \begin{pmatrix} \cos \phi_m \\ \sin \phi_m \\ 0 \end{pmatrix}, \quad (2)$$

and

$$\mathbf{m}_i = \begin{pmatrix} \cos(\phi_i) \\ \sin(\phi_i) \\ 0 \end{pmatrix} = \begin{pmatrix} \cos(-\phi_m - \frac{2\pi i}{3} + \eta_i) \\ \sin(-\phi_m - \frac{2\pi i}{3} + \eta_i) \\ 0 \end{pmatrix}, \quad (3)$$

where $u_m = \|\mathbf{m}\|$, ϕ_m is the azimuthal angle corresponding to \mathbf{m} , $i = \{1, 2, 3\}$, while η_i is the small deviation from the perfect $\frac{2\pi}{3}$ ordering (*i.e.* $\eta_i \ll \frac{2\pi}{3}$). They are defined such that

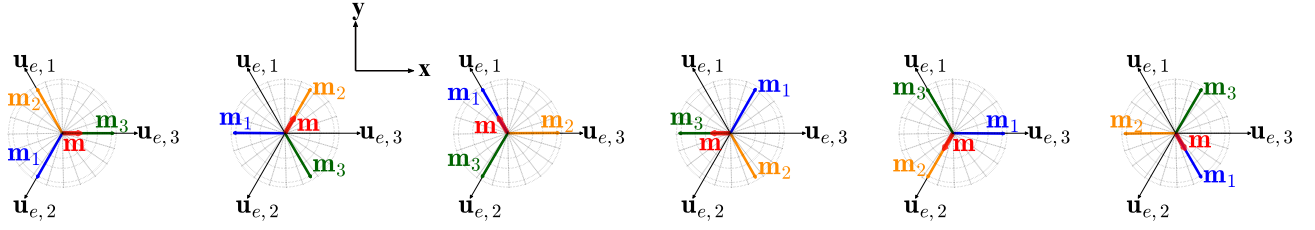


FIG. 2. Six possible equilibrium states in single domain Mn₃Sn crystal. They lie in the Kagome plane, which is assumed to coincide with the x-y plane, and are separated from each other by 60 degrees. In each case, only one of the sublattice vectors, \mathbf{m}_i , coincides with its easy axis, $\mathbf{u}_{e,i}$. A small in-plane average magnetization, \mathbf{m} , also coincides with this particular \mathbf{m}_i and its corresponding easy axis. Here, \mathbf{m} is not drawn to scale but magnified by 100 \times for the purpose of clear representation.

$\eta_1 + \eta_2 + \eta_3 = 0$. Using the perturbative approach, also presented in the supplementary material, we find

$$\eta_1 \approx \frac{K_e}{3(J_E + \sqrt{3}D)} \left(\sqrt{3} \cos(2\varphi_m) - \sin(2\varphi_m) \right), \quad (4a)$$

$$\eta_2 \approx -\frac{K_e}{3(J_E + \sqrt{3}D)} \left(\sqrt{3} \cos(2\varphi_m) + \sin(2\varphi_m) \right), \quad (4b)$$

which is then used to obtain u_m as

$$u_m = \frac{K_e}{3(J_E + \sqrt{3}D)}. \quad (5)$$

On further analysis we obtain the energy density as

$$F(\varphi_m) \approx -\frac{(3J_E + 7\sqrt{3}D)K_e^3}{18(J_E + \sqrt{3}D)^3} \cos(6\varphi_m), \quad (6)$$

where the constant energy terms are not shown. This $\cos(6\varphi_m)$ dependence explains the six minimum energy states shown in Fig. 2. We find the analytic expressions of Eqs. (4) and (5) to match very well against the numerical results (presented in supplementary material).

IV. SOT-DRIVEN DYNAMICS

The setup used for analyzing the dynamics of the antiferromagnet when subject to SOT is shown in Fig. 3. The spin current generated due to charge-to-spin conversion in the heavy metal is polarized along \mathbf{n}_p , which coincides with z-axis, per our convention. The Kagome lattice of Mn₃Sn is formed in the x-y plane while the z-axis coincides with [0001] direction, as shown in Fig. 1(b). This setup resembles the experimental setup from Refs. 33, 46, where an MgO (110)[001] substrate leads to the selective growth of Mn₃Sn in [0001] direction. The effect of SOT on the AFM order is maximum in this setup since the sublattice vectors predominantly lie in the x-y plane with small z-component while the spin polarization is perpendicular to the x-y plane.³³ Other methods of spin injection, such as a spin-polarized electric current from a proximal ferromagnet, could also be used. As mentioned previously, our analysis of the SOT dynamics will be carried out in the single-domain limit.

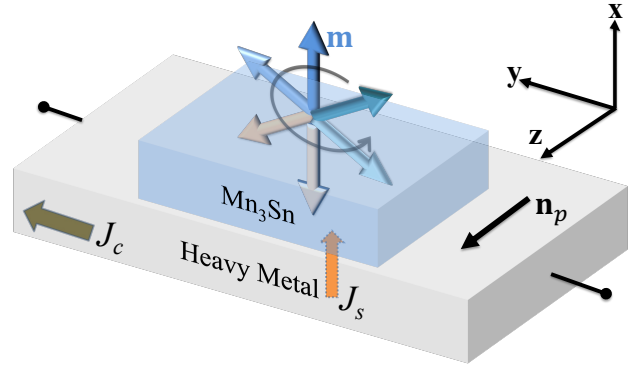


FIG. 3. Device setup for manipulating the magnetic state in Mn₃Sn. Spin-orbit torque, which is generated due to the spin-Hall effect in the heavy metal, is utilized to manipulate the state of the thin layer of Mn₃Sn. \mathbf{m} is the small but nonzero net magnetization in Mn₃Sn. J_c and J_s are the charge current density and spin current density, respectively.

For each sublattice of Mn₃Sn, the magnetization dynamics is governed by the classical Landau-Lifshitz-Gilbert (LLG) equation, which is a statement of the conservation of angular momentum. The LLG equations for the sub-lattices are coupled via the exchange interaction. For sublattice i , the LLG equation is given as⁵²

$$\begin{aligned} \dot{\mathbf{m}}_i = & -\gamma\mu_0 \left(\mathbf{m}_i \times \mathbf{H}_i^{\text{eff}} \right) + \alpha \left(\mathbf{m}_i \times \dot{\mathbf{m}}_i \right) \\ & - \frac{\hbar}{2e} \frac{\gamma J_s}{M_s d_a} \mathbf{m}_i \times \left(\mathbf{m}_i \times \mathbf{n}_p \right), \end{aligned} \quad (7)$$

where $\dot{\mathbf{m}}_i = \frac{\partial \mathbf{m}_i}{\partial t}$, t is time in seconds, $\mathbf{H}_i^{\text{eff}}$ is the effective magnetic field experienced by \mathbf{m}_i , α is the Gilbert damping parameter for Mn₃Sn, J_s is the input spin current density with spin polarization along $\mathbf{n}_p = \mathbf{z}$, and d_a is the thickness of the AFM layer. Other parameters in this equation, viz. $\hbar = 1.054561 \times 10^{-34}$ J.s, $\mu_0 = 4\pi \times 10^{-7}$ N/A², $e = 1.6 \times 10^{-19}$ C, and $\gamma = 17.6 \times 10^{10}$ T⁻¹s⁻¹ are the reduced Planck's constant, the permeability of free space, the elementary charge of an electron, and the gyromagnetic ratio, respectively. The spin current density depends on the input charge

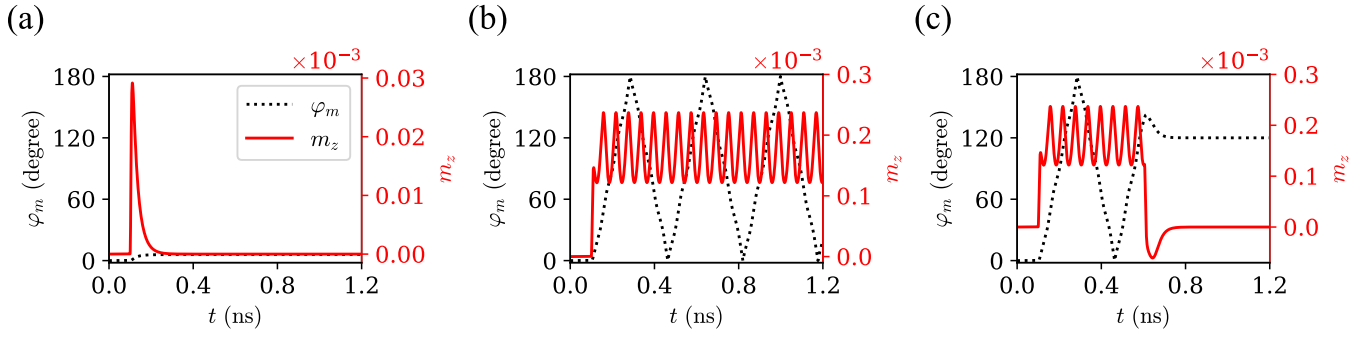


FIG. 4. Response of order parameter \mathbf{m} to different spin currents. (a) Non-equilibrium stationary steady-state solution for $J_s = 0.1 \text{ MA/cm}^2$. This current is below the threshold current. (b) Oscillatory steady-state dynamics for DC current $J_s = 0.5 \text{ MA/cm}^2$. (c) Switching dynamics for current pulse of magnitude $J_s = 0.5 \text{ MA/cm}^2$ and duration $t_{pw} = 500 \text{ ps}$. For both (b) and (c) $J_s > J_s^{\text{th}}$. Here, the thickness of the AFM layer, $d_a = 4 \text{ nm}$ and $J_s^{\text{th}} \approx 1.7 \text{ MA/cm}^2$.

current density, J_c , and the spin-Hall angle of the heavy metal (HM), θ_{SH} , as $J_s = \theta_{\text{SH}} J_c$. The spin-Hall angle is associated with the efficiency of the SOT effect. A recent experiment⁴⁸ on switching dynamics in Mn₃Sn estimated a large (small) and negative (positive) θ_{SH} in W (Pt). Subsequent experiments^{34,46} have also preferred W as the heavy metal in their SOT switching experiments; therefore, in this work we consider the HM to be W. Its properties are reported in Table I.

The effective magnetic field for sublattice i can be obtained by using Eq. (1) as

$$\mathbf{H}_i^{\text{eff}} = -\frac{1}{\mu_0 M_s} \frac{\partial F}{\partial \mathbf{m}_i} = -\frac{J_E}{\mu_0 M_s} (\mathbf{m}_j + \mathbf{m}_k) + \frac{D\mathbf{z} \times (\mathbf{m}_j - \mathbf{m}_k)}{\mu_0 M_s} + \frac{2K_e}{\mu_0 M_s} (\mathbf{m}_i \cdot \mathbf{u}_{e,i}) \mathbf{u}_{e,i} + \mathbf{H}_a, \quad (8)$$

where $(i, j, k) = (1, 2, 3), (2, 3, 1),$ or $(3, 1, 2)$, respectively. For all the numerical results presented in this work, Eqs. (7) and (8) are solved simultaneously with $\varphi_m^i = 0$ as the initial state. The results would be equally applicable if any of the other five equilibrium states were considered as the initial state. The dynamic instability caused in the order parameters depends on the magnitude of the SOT relative to the intrinsic energy scale of the AFM. Numerical simulations of the coupled LLG equations show that when the input spin current density (J_s) is below a certain threshold current (J_s^{th}), the order parameters evolve to a non-equilibrium stationary steady-state in the Kagome plane, as shown in Fig. 4(a). However, the z-component of the order parameters in the stationary steady-states is zero. On the other hand, if $J_s > J_s^{\text{th}}$, the order parameters exhibit oscillatory dynamics, as shown in Fig. 4(b). The oscillation frequency can be tuned from the GHz to the THz range, depending on the magnitude of J_s relative to J_s^{th} . Finally, Fig. 4(c) shows that if the current is turned off during the oscillatory dynamics, the system could switch to one of the six equilibrium states, φ_m^{eq} . Different final states can be achieved by tuning the duration or the magnitude of the current pulse.

A. Stationary states and threshold current

In order to analytically evaluate the threshold current and the stationary state solutions, we consider \mathbf{m} as that given by Eq. (2), since our numerical result in Fig. 4(a) indicates it to be in the Kagome plane. Next, we evaluate $\dot{\mathbf{m}} = \frac{(\dot{\mathbf{m}}_1 + \dot{\mathbf{m}}_2 + \dot{\mathbf{m}}_3)}{3}$ as⁵¹

$$\dot{\mathbf{m}} = -\frac{\gamma \mu_0}{3} (\mathbf{m}_1 \times \mathbf{H}_1^{\text{eff}} + \mathbf{m}_2 \times \mathbf{H}_2^{\text{eff}} + \mathbf{m}_3 \times \mathbf{H}_3^{\text{eff}}) + \frac{\alpha}{3} (\mathbf{m}_1 \times \dot{\mathbf{m}}_1 + \mathbf{m}_2 \times \dot{\mathbf{m}}_2 + \mathbf{m}_3 \times \dot{\mathbf{m}}_3) - \frac{1}{3} \frac{\hbar}{2e} \frac{\gamma J_s}{M_s d_a} \times (\mathbf{m}_1 \times (\mathbf{m}_1 \times \mathbf{z}) + \mathbf{m}_2 \times (\mathbf{m}_2 \times \mathbf{z}) + \mathbf{m}_3 \times (\mathbf{m}_3 \times \mathbf{z})), \quad (9)$$

and then simplify it to

$$\dot{\mathbf{m}} = -\frac{\gamma}{3M_s} \frac{\partial F}{\partial \varphi_m} \mathbf{z} - \alpha \dot{\varphi}_m \mathbf{z} + \frac{\hbar}{2e} \frac{\gamma J_s}{M_s d_a} \mathbf{z}, \quad (10)$$

where we have used $\mathbf{m}_i \times \mathbf{H}_i^{\text{eff}} = \frac{-1}{\mu_0 M_s} \frac{\partial F}{\partial \varphi_i} \mathbf{z} = \frac{-1}{\mu_0 M_s} \frac{\partial F}{\partial \varphi_m} \frac{\partial \varphi_m}{\partial \varphi_i} \mathbf{z} = \frac{1}{3\mu_0 M_s} \frac{\partial F}{\partial \varphi_m} \mathbf{z}$. Since the steady-state z-component of \mathbf{m} must be zero for currents below the threshold current, the net torque is zero in the z-direction viz., $\dot{m}_z = 0$. Therefore, we have

$$\alpha \dot{\varphi}_m = -\frac{\gamma}{M_s} \frac{(3J_E + 7\sqrt{3}D)K_e^3}{9(J_E + \sqrt{3}D)^3} \sin(6\varphi_m) + \frac{\hbar}{2e} \frac{\gamma J_s}{M_s d_a}. \quad (11)$$

When the spin current is turned on, the energy of the order parameters increases, and they drift away from their equilibrium state. The intrinsic damping of the system, however, dissipates some of the supplied energy. If the net energy is less than that required to overcome the intrinsic energy barrier, the system settles to a non-equilibrium steady-state, where the antidamping torque due to the spin current is balanced by the torque due to the internal field. Therefore, $\dot{\mathbf{m}} = 0$, $\dot{\varphi}_m = 0$, and the non-equilibrium stationary steady-states are given as

$$\varphi_m^{\text{st}} = \varphi_m^{\text{eq}} + \frac{1}{6} \sin^{-1} \left(\frac{\frac{\hbar}{2e} \frac{J_s}{d_a}}{\frac{(3J_E + 7\sqrt{3}D)K_e^3}{9(J_E + \sqrt{3}D)^3}} \right), \quad (12)$$

where adding ϕ_m^{eq} ensures that the above equation is valid irrespective of the initial equilibrium state. The stationary state of the system as a function of the input spin current density ($J_s < J_s^{\text{th}}$) is shown in Fig. 5 for different AFM thicknesses. It shows excellent agreement between the analytic model of Eq. (12) and that obtained from the numerical simulation of Eq. (7) for all AFM thicknesses examined here. These results should be widely applicable as long as the thickness of the AFM film is within the single-domain limit.^{46,47} In general, ϕ_m^{st} increases with input current since higher current injects more energy and the order parameter moves further away from its equilibrium orientation. Finally, the threshold current corresponds to J_s which makes the argument of $\sin^{-1}(\cdot)$ in Eq. (12) equal to ± 1 . It is, therefore, given as

$$J_s^{\text{th}} = d_a \frac{2e}{\hbar} \frac{(3J_E + 7\sqrt{3}D)K_e^3}{9(J_E + \sqrt{3}D)^3}. \quad (13)$$

It corresponds to the minimum current that pushes the order parameter above the energy barrier. As expected, the strength of J_s^{th} depends on the effective energy barrier imposed by the intrinsic energy interactions (Eq. (6)). Similar expressions have also been obtained in case of collinear and non-collinear AFMs with two-fold anisotropy,^{6,10,12,14,38,45} however, prior works have not addressed the case of the six-fold anisotropy in materials like Mn₃Sn and Mn₃Ge.

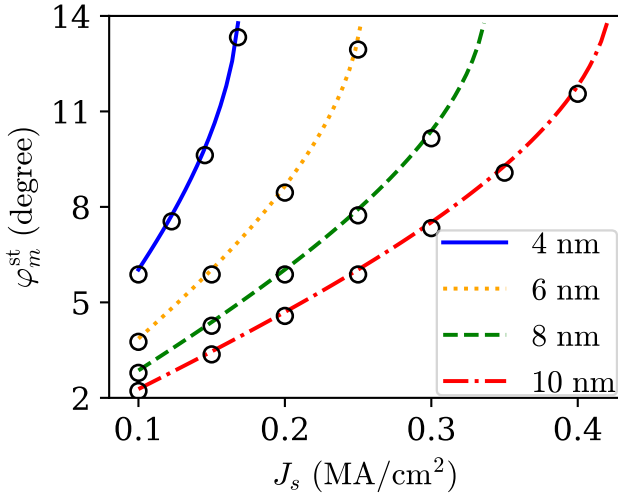


FIG. 5. Non-equilibrium stationary steady-states as a function of the applied spin current J_s for different thickness of the Mn₃Sn layer. The applied current is below the threshold current in each case. Numerical result from the solution of Eq. (7) (symbols) fully agree with the analytical results obtained from Eq. (12) (lines).

B. Oscillation dynamics under DC SOT

For currents above the threshold current ($J_s > J_s^{\text{th}}$), the net energy pumped into the system overcomes the intrinsic barrier imposed by the effective anisotropy of the system. The z-component of the order parameter increases due to the SOT,

as shown in Fig. 4(b). For the case of the spin polarization perpendicular to the kagome plane, as considered in this work, an equal spin torque acts on all the sublattice vectors along the z-direction.^{46,51} As a result, their z-components increase in magnitude, which in turn increases the z-component of the average magnetization since $m_z = (m_{1,z} + m_{2,z} + m_{3,z})/3$. Consequently, an effective exchange field ($\propto J_E m_z$) arises in the z-direction, which leads to oscillation of the order parameters around the z-axis with frequencies in the GHz-THz range.^{14,44}

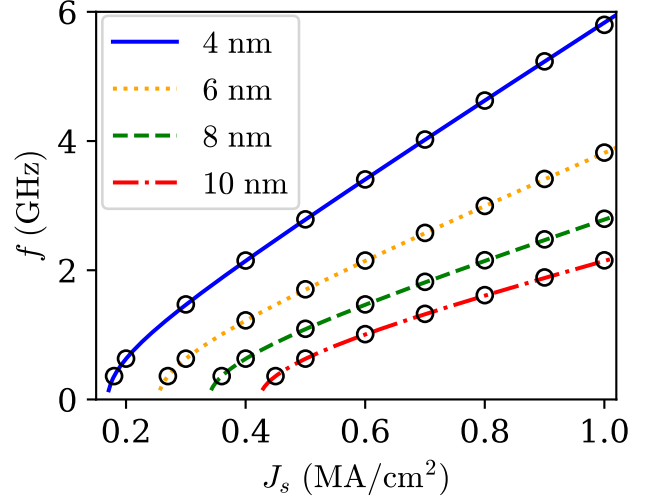


FIG. 6. Oscillation frequency as a function of the applied spin current J_s for different thickness of the Mn₃Sn layer. The applied current is above the threshold current in each case. Numerical result from the solution of Eq. (7) (symbols) agree very well with the analytical results obtained from Eq. (14) (lines).

For currents close to the threshold current ($J_s \gtrsim J_s^{\text{th}}$), m_z is small, as shown in Fig. 4(b). It depends on ϕ_m and the exchange constant as $m_z \approx -\frac{\phi_m}{3\gamma J_E/M_s}$,^{14,44} while our numerical simulations reveal that $\frac{m_z}{\alpha\phi_m} < 0.1$. Therefore, we can use Eq. (11) to obtain the time period for 2π rotation as

$$\begin{aligned} \frac{1}{f} &= \alpha \frac{2e}{\hbar} \frac{M_s d_a}{\gamma J_s} \int_{\phi_{m,0}}^{\phi_{m,0}+2\pi} \frac{d\phi_m'}{1 - \left(\frac{J_s^{\text{th}}}{J_s}\right) \sin(6\phi_m')} \\ &= \frac{\alpha \frac{2e}{\hbar} \frac{M_s d_a}{\gamma J_s}}{3\sqrt{1 - \left(\frac{J_s^{\text{th}}}{J_s}\right)^2}} \tan^{-1} \left(\frac{\tan(3\phi_m') - \frac{J_s^{\text{th}}}{J_s}}{\sqrt{1 - \left(\frac{J_s^{\text{th}}}{J_s}\right)^2}} \right) \Bigg|_0^{2\pi} \\ &= \alpha \frac{2e}{\hbar} \frac{M_s d_a}{\gamma J_s} \frac{2\pi}{\sqrt{1 - \left(\frac{J_s^{\text{th}}}{J_s}\right)^2}}, \end{aligned} \quad (14)$$

where we assumed $\phi_{m,0} = 0$. Figure 6 shows the frequency of oscillation of the order parameter, f , as a function of the spin current density for different AFM thicknesses, d_a . Firstly, for each AFM thickness, f increases with J_s since more energy is pumped into the system. Secondly, at any current, f decreases with d_a since the strength of spin torque is inversely propor-

tional to d_a . Finally, numerical values of frequency obtained from the solution of Eq. (7) (symbols) match very well against the results of Eq. (14) (lines), thereby showing the efficacy of our models. The results suggest that close to the threshold current f scales as $\sim J_s^{\text{th}} \sqrt{\left(\frac{J_s}{J_s^{\text{th}}}\right)^2 - 1}$, whereas f increases almost linearly with J_s for $J_s \gg J_s^{\text{th}}$. This linear scaling of frequency with the input current has also been suggested in previous works,^{14,33} however, the dependence of the f on the six-fold anisotropy has not been discussed previously.

C. Switching dynamics under pulsed SOT

If the input spin current is turned off during the course of the oscillation, the order parameter loses energy to the intrinsic damping of the AFM. As a result, m_z reduces to zero, while φ_m settles into the nearest equilibrium state, as shown in Fig. 4(c). Here, $\pi/2 < \varphi_m < 5\pi/6$ when the current is turned off; therefore, the order parameter settles into $\varphi_m^{\text{eq}} = 2\pi/3$ equilibrium state. Comparing Figs. 4(b) and 4(c), one can conclude that it is possible to switch to all six states, if the current pulse is switched off at an appropriate time. Indeed the same is shown in Fig. 7, where different final states are achieved by changing the duration of the current pulse of magnitude $J_s = 0.6 \text{ MA/cm}^2$. Another way to switch between stable states is by varying the magnitude of current pulse for a fixed duration. Figure 8 shows switching of the order parameter from $\varphi_m^{\text{eq}} = 0$ to $\varphi_m^{\text{eq}} = \pi/3, 2\pi/3$ and π as the magnitude of the input current is increased, while its duration is fixed at 100 ps. In Figs. 7 and 8, we only present switching in one direction, that is from $\varphi_m^{\text{eq}} = 0$ through $\varphi_m^{\text{eq}} = \pi$ since $\varphi_m^{\text{eq}} = 4\pi/3$ and $\varphi_m^{\text{eq}} = 5\pi/3$ could be achieved by changing the direction of input current. Finally, $m_z(\infty - \dot{\varphi}_m)$ increases both in magnitude and frequency with J_s (Fig. 8(b)) since φ_m increases with current (Eq. 11).

Increasing either the magnitude or the duration of the current pulse increases the input energy to the order parameter. As a result, it starts a precessional motion till the current pulse is turned off, after which it loses its energy to the intrinsic damping and reaches an equilibrium state. The final state could, therefore, be considered a function of the net input energy. For low energy switching operation between two equilibrium states, the net input energy should be just enough to move the order parameter to the top of a barrier preceding the final equilibrium state, thereafter the intrinsic damping of the system assists in the switching process. To determine the duration (t_{pw}) and magnitude (J_s) of the current pulse required to switch from $\varphi_m^{\text{eq}} = 0$ to $\varphi_m^{\text{eq}} = n\pi/3$ ($n = \{1, 2, 3\}$), we use Eq. (11). We find that t_{pw} and J_s required to switch to a different state depends on the final state as

$$J_s t_{\text{pw}} = \alpha \frac{2e}{\hbar} \frac{M_s d_a}{\gamma} \frac{\frac{(2n-1)\pi}{2} + \tan^{-1}\left(\frac{J_s^{\text{th}}/J_s}{\sqrt{1-(J_s^{\text{th}}/J_s)^2}}\right)}{3\sqrt{1-(J_s^{\text{th}}/J_s)^2}}. \quad (15)$$

This equation suggests that for large currents ($J_s \gg J_s^{\text{th}}$), the final equilibrium state depends only on the input spin charge

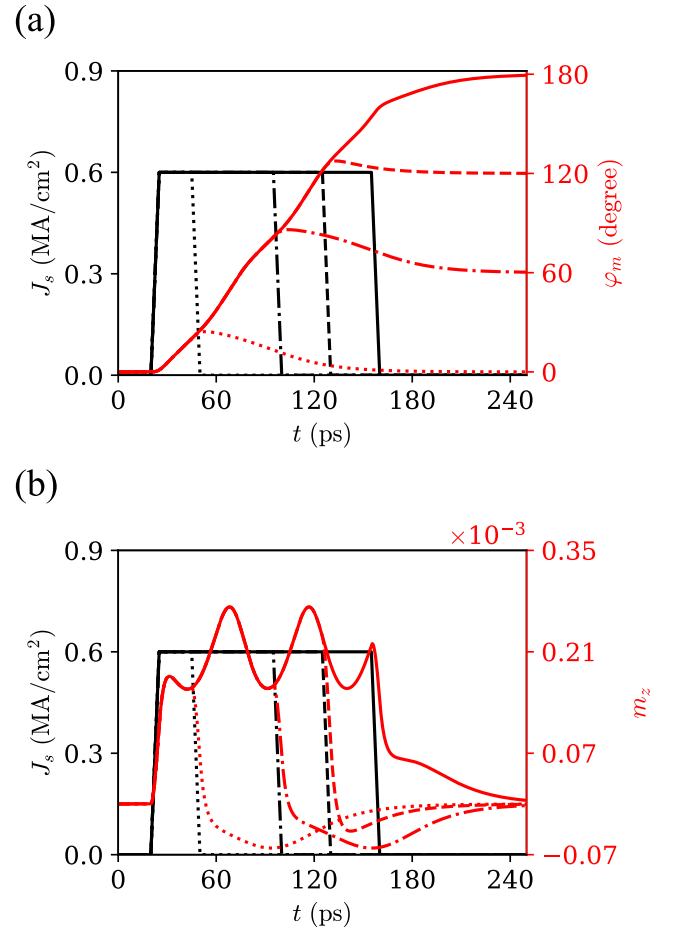


FIG. 7. The response of single domain Mn₃Sn to a current pulse of fixed amplitude of 0.6 MA/cm^2 but different duration. Left axis: Magnitude of current pulses, with rise and fall time of 5 ps each. Right axis: (a) The azimuthal angle, φ_m , as a function of time. (b) The z-component of the average magnetization, m_z , as a function of time. φ_m can be switched from its initial state ($\varphi_m^{\text{eq}} = 0$) to a different state, if the net input energy (tuned by varying t_{pw}) overcomes the effective potential barrier. As pulse duration increases m_z stays non-zero for longer period.

density ($J_s t_{\text{pw}}$) as $J_s t_{\text{pw}} \sim \alpha \frac{2e}{\hbar} \frac{M_s d_a}{\gamma} \frac{(2n-1)\pi}{6}$. Such a large current density above the threshold current density corresponds to the small pulse width regime. For current magnitude near the threshold current ($J_s \gtrsim J_s^{\text{th}}$) and large t_{pw} , the final state scales

almost linearly with t_{pw} as $J_s^{\text{th}} t_{\text{pw}} \sqrt{\left(\frac{J_s}{J_s^{\text{th}}}\right)^2 - 1} \sim \alpha \frac{2e}{\hbar} \frac{M_s d_a}{\gamma} \frac{n\pi}{3}$.

To verify these claims, we solved Eq. (7) for t_{pw} in the range [1, 100] ps and spin charge density in the range [0, 1] C/m², and evaluated the final states. It can be observed from Fig. 9 that for small t_{pw} , the final states (φ_m^{eq}) is indeed dependent only on $J_s t_{\text{pw}}$, more evidently for $\varphi_m^{\text{eq}} = 2\pi/3$ and π . This is because the input current is large for these cases. On the other hand, the final states for large pulse width clearly depends on t_{pw} . This behavior is more noticeable for $\varphi_m^{\text{eq}} = \pi/3$ and $\varphi_m^{\text{eq}} = 2\pi/3$ whereas for $\varphi_m^{\text{eq}} = \pi$, it would be evident for longer pulse widths. The overlaid dashed lines correspond to

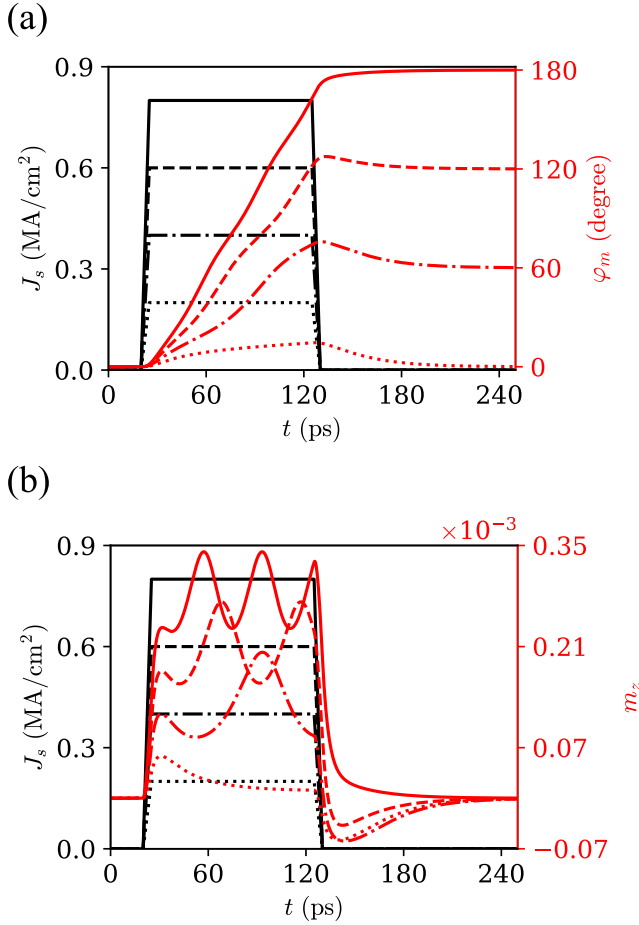


FIG. 8. The response of single domain Mn₃Sn to a current pulse of fixed duration of 100 ps, but different amplitudes. Left axis: Magnitude of current pulses, with rise and fall time of 5 ps each. Right axis: (a) The azimuthal angle, φ_m , as a function of time. (b) The z-component of the average magnetization, m_z , as a function of time. φ_m can be switched from its initial state ($\varphi_m^{\text{eq}} = 0$) to a different state, if the net input energy (tuned by varying J_s) overcomes the effective potential barrier. m_z increases, both in magnitude and frequency, with increase in the pulse amplitude.

Eq. (15) for $n = 1, 2, 3$ and represent the minimum spin charge density required to switch from $\varphi_m^{\text{eq}} = 0$ to $\varphi_m^{\text{eq}} = n\pi/3$ as a function of the pulse width. The fluctuations of the Hall resistance under the effect of SOT in Ref. 33 were credited to the aforementioned pulsed dynamics. However, an expression describing the interdependence of J_s and t_{pw} required to switch from one known state to another known state, as a function of the material parameters, was missing.

V. READOUT OF MAGNETIC STATE

A. Anomalous Hall Effect

Non-collinear AFMs, such as Mn₃Sn, exhibit non-zero AHE due to the non-zero Berry curvature in the momentum space when certain symmetries are absent.²⁶ In a Hall bar

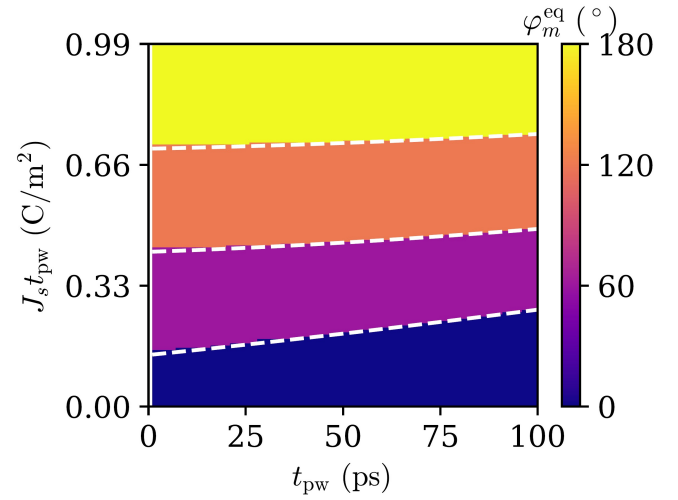


FIG. 9. The final state of \mathbf{m} as a function of the pulse duration, t_{pw} , and the total injected spin charge density, $J_s t_{\text{pw}}$. The overlaid dashed white lines represent the analytic bounds of Eq. (15). Here, the thickness of the AFM film is $d_a = 4$ nm.

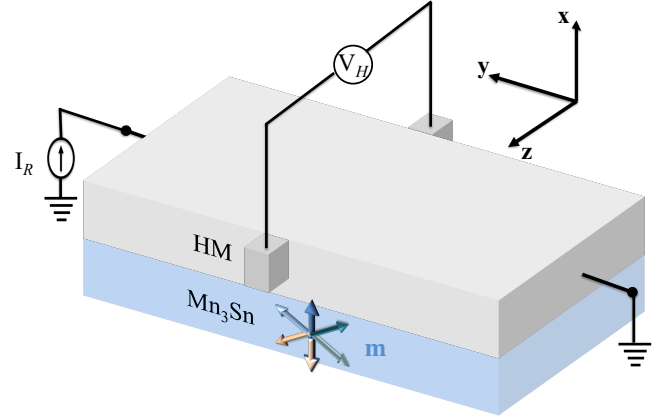


FIG. 10. A Hall bar setup to measure the output voltage signal, V_H , generated on the injection of charge read current, I_R . This current is lower than the threshold current to induce dynamics, I_c^{th} . The arrows show different orientations of \mathbf{m} .

setup, a read current (I_R) lower than the threshold charge current (I_c^{th}) to induce dynamics, is applied to a bilayer of the heavy metal and Mn₃Sn, as shown in Fig. 10. A voltage (V_H) transverse to the current flow is measured to detect the magnetization state of Mn₃Sn. Since this voltage depends on the Hall resistance of the Mn₃Sn layer, $R_H^{\text{Mn}_3\text{Sn}}$, it is given as^{46,53}

$$V_H = I_R \left(1 + \frac{\rho_{\text{Mn}_3\text{Sn}}}{\rho_{\text{HM}}} \frac{d_{\text{HM}}}{d_{\text{Mn}_3\text{Sn}}} \right)^{-2} R_H^{\text{Mn}_3\text{Sn}}, \quad (16)$$

where $\rho_{\text{Mn}_3\text{Sn}}$ (ρ_{HM}) and $d_{\text{Mn}_3\text{Sn}}$ (d_{HM}) are the electrical resistivity and thickness of the Mn₃Sn (HM) layer, respectively. The Hall resistance of Mn₃Sn depends on the Hall resistivity $\rho_H^{\text{Mn}_3\text{Sn}}$, and is given as $R_H^{\text{Mn}_3\text{Sn}} = \frac{\rho_H^{\text{Mn}_3\text{Sn}}}{d_{\text{Mn}_3\text{Sn}}}$.

In the above equation, the magnitude of current leakage into the AFM layer is evaluated assuming a parallel resistance combination of the heavy metal and the AFM layers, as $I_R^{\text{Mn}_3\text{Sn}} = I_R \left(1 + \frac{\rho_{\text{Mn}_3\text{Sn}}}{\rho_{\text{HM}}} \frac{d_{\text{HM}}}{d_{\text{Mn}_3\text{Sn}}}\right)^{-1}$. On the other hand, the transverse Hall voltage can be obtained as $V_H = V_H^{\text{Mn}_3\text{Sn}} \left(1 + \frac{\rho_{\text{Mn}_3\text{Sn}}}{\rho_{\text{HM}}} \frac{d_{\text{HM}}}{d_{\text{Mn}_3\text{Sn}}}\right)^{-1}$, where the bilayer is assumed as two resistances connected in series.

To calculate the Hall voltage in our device setup, we consider $\rho_{\text{HM}} = 43.8 \mu\Omega \cdot \text{cm}$ and $d_{\text{HM}} = 7 \text{ nm}$, corresponding to that of W (listed in Table I), while the other parameters are taken as $\rho^{\text{Mn}_3\text{Sn}} = 330 \mu\Omega \cdot \text{cm}$,³³ $d_{\text{Mn}_3\text{Sn}} = 4 \text{ nm}$, and $|\rho_H^{\text{Mn}_3\text{Sn}}| = 3 \mu\Omega \cdot \text{cm}$.⁵⁴ If a read current of $I_R = 50 \mu\text{A}$ is applied to the bilayer, a Hall voltage of $V_H = 1.86 \mu\text{V}$ is generated in the HM layer. As indicated in Eq. (16), a larger read current would increase⁵³ the detected Hall voltage. Alternatively, a larger Hall resistivity of Mn₃Sn would be desired to generate larger read voltages. Since the read and write terminals in this device setup are same, this setup is more suitable for detecting the switching dynamics.

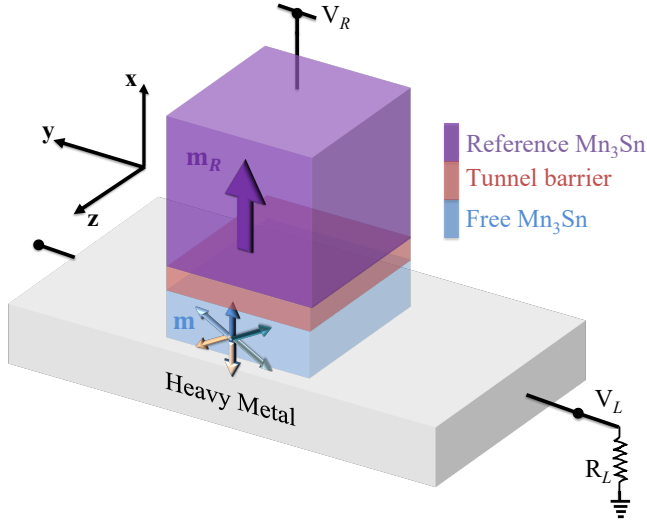


FIG. 11. All antiferromagnetic tunnel junction atop the heavy metal layer. Both the reference and free layers are composed of Mn₃Sn. The arrows in free Mn₃Sn show the six equilibrium orientations of \mathbf{m} while that in reference Mn₃Sn shows the fixed orientation of its order parameter, \mathbf{m}_R . A small read voltage, V_R , is applied and a voltage, V_L , is detected across the resistive load, R_L . V_L depends on the orientation of \mathbf{m} with respect to \mathbf{m}_R .

B. Tunneling Magnetoresistance

An all antiferromagnetic tunnel junction built using two Mn₃Sn electrodes has recently been shown to exhibit a finite TMR at room temperature.³⁶ It was experimentally demonstrated that a TMR value of about 2% at room temperature was possible for thicker tunnel barrier (MgO) and large resistance-area (RA) product. The high (low) resistance state corresponds to an angle of $\pi(0)$ between the magnetic octupoles of

the two Mn₃Sn layers. The electronic bands in Mn₃Sn show momentum-dependent spin splitting of the Fermi surface due to the broken time reversal symmetry.^{36,55} As a result, a spin-polarized current is generated. The relative orientation of the magnetic octupoles in the two AFM layers controls the magnitude of the spin-polarized current, and hence the magnetoresistance.⁵⁵ A simple representation of an all-Mn₃Sn tunnel junction is shown in Fig. 11. Here, a thick layer of Mn₃Sn, with fixed orientation \mathbf{m}_R , is used as the reference layer, while the order parameter \mathbf{m} of the thinner layer is modulated using the device setup of Fig. 3. The different orientations of \mathbf{m} with respect to \mathbf{m}_R is measured as the read voltage, V_L , across a resistive lead, R_L , resulting in a finite read voltage, V_R .

Theoretical calculations have revealed that for vacuum as a tunnel barrier, RA product increased from approximately $0.05 \Omega \cdot \mu\text{m}^2$ in the parallel configuration to $0.2 \Omega \cdot \mu\text{m}^2$ in the antiparallel configuration.⁵⁵ For the states corresponding to $\phi_m^{\text{eq}} = \pi/3$ and $\phi_m^{\text{eq}} = 2\pi/3$, the RA product is evaluated to be approximately $0.07 \Omega \cdot \mu\text{m}^2$ and $0.11 \Omega \cdot \mu\text{m}^2$, respectively.⁵⁵ Assuming the same value of RA product in our device setup, we estimate the voltage drop across $R_L = 50 \Omega$ as $V_L = 9.1 \text{ mV}$ for the parallel configuration, while $V_L = 7.1 \text{ mV}$ for the antiparallel configuration of the free and fixed layers of the tunnel junction. On the other hand, $V_L = 8.8 \text{ mV}$ and $V_L = 8.2 \text{ mV}$ for $\phi_m^{\text{eq}} = \pi/3$ and $\phi_m^{\text{eq}} = 2\pi/3$, respectively. Here, we considered $V_R = 10 \text{ mV}$ while the area of the tunnel barrier was assumed to be $\mathcal{A} = 100 \times 100 \text{ nm}^2$. This setup can be used for detecting both the oscillation and switching dynamics.

VI. CONSIDERATION OF THERMAL EFFECTS

When Mn₃Sn is driven by large DC SOT to excite oscillatory dynamics in the 100's of GHz range, it is likely that Joule heating in the device structure would impose practical limits on the operating conditions. For example, our simulations show that we need approximately 17 MA/cm^2 spin current to generate oscillations of the order parameter at 100 GHz in a 4 nm thick film of Mn₃Sn. Due to the spin Hall angle of heavy metal being less than unity, the required charge current could be 2-20× higher than the spin current. The large charge current requirement will increase the temperature of the device structure, which, if significant, could alter the properties of the magnetic material, or in extreme cases change the magnetic order completely. In addition to the magnitude of the input current pulse, the Joule heating in the device also depends on the electrical properties and the size of the heavy metal that the charge current passes through. The temperature rise of the device due to the generated heat depends on the ambient temperature and the thermal properties of the conducting (magnetic and non-magnetic) media and the substrate. Finally, in the pulsed response case, the time-domain temperature profile is expected to be sensitive to the duration of the applied current and thus the peak temperature in this case could be markedly different from that achieved when DC charge currents are used in the device.

Recent experimental investigation of field-assisted current-driven switching dynamics in Mn₃Sn attribute the switching

process to Joule heating.^{34,35} They show that despite the spin diffusion length in Mn₃Sn being extremely small (roughly 1 nm), the measured AHE signals showed switching behavior for films of thicknesses ranging from 30 nm to 100 nm. Subsequently, this switching dynamics was explained as a demagnetization of the AFM order in Mn₃Sn due to Joule heating over a time scale of 10's of nanosecond (ns), followed by a remagnetization of the AFM order due to cooling in the presence of SOT. We must, however, point out that the SOT device setups in these experiments were different from our setup of Fig. 3. Unlike our case, the spin polarization associated with the SOT was in the Kagome plane, which increases the current requirement.^{33,46} Nevertheless, an accurate investigation of the current-driven magnetization dynamics in our device setup, requires a careful consideration of the temperature rise due to Joule heating.

To investigate the temperature rise in our setup, we assume a one-dimensional heat flow into the substrate (MgO), as presented in Ref. 56. Consequently, the junction temperature is strongly depended on the properties of the substrate such as its thermal conductivity $\kappa_{\text{sub}} = 40 \text{ W}/(\text{m} \cdot \text{K})$, thickness d_{sub} , mass density $\rho_{\text{sub}} = 3580 \text{ kg}/\text{m}^3$, and specific heat capacity $C_{\text{sub}} = 930 \text{ J}/(\text{kg} \cdot \text{K})$. These values are taken from Ref. 57. In our model, we assume that the HM and Mn₃Sn are at the same temperature and that the temperature is spatially invariant in the bilayer. The area of the heat source is set by the dimensions, i.e., the length and the width, of the bilayer. The rise in the junction temperature, $\Delta T_j(t)$, is then calculated as⁵⁶

$$\Delta T_j(t) = \Delta T_M \left(\left(1 - \frac{8}{\pi^2} \sum_{k=\text{odd}} \frac{\exp(-k^2 t / \tau)}{k^2} \right) - \theta(t - t_{\text{pw}}) \left(1 - \frac{8}{\pi^2} \sum_{k=\text{odd}} \frac{\exp(-k^2(t - t_{\text{pw}}) / \tau)}{k^2} \right) \right), \quad (17)$$

where

$$\Delta T_M = \frac{d_{\text{sub}} J_c^2}{\kappa_{\text{sub}}} \frac{\left(\rho_{\text{Mn}_3\text{Sn}} d_{\text{Mn}_3\text{Sn}} + \left(\frac{\rho_{\text{Mn}_3\text{Sn}}}{\rho_{\text{HM}}} \frac{d_{\text{HM}}}{d_{\text{Mn}_3\text{Sn}}} \right)^2 \rho_{\text{HM}} d_{\text{HM}} \right)}{\left(1 + \frac{\rho_{\text{Mn}_3\text{Sn}}}{\rho_{\text{HM}}} \frac{d_{\text{HM}}}{d_{\text{Mn}_3\text{Sn}}} \right)^2} \quad (18)$$

is the maximum possible rise in the junction temperature for an input charge current density, J_c , and includes the current leakage into the Mn₃Sn layer (as described in Section V A). The rate of the heat flow into the substrate is determined by the thermal rate constant, $\tau = \frac{4d_{\text{sub}}^2 \rho_{\text{sub}} C_{\text{sub}}}{\pi^2 \kappa_{\text{sub}}}$. Finally, $\theta(\cdot)$ in Eq. (17) is the Heaviside step function.

Figure 12 shows the maximum rise in the junction temperature for different substrate thicknesses and DC input charge current densities. As expected, ΔT_M increases with both d_{sub} and J_c . An increase in J_c , increases the heat generated in the metallic layers, whereas an increase in d_{sub} , increases the thermal resistance in the direction of heat flow. Assuming the heat sink temperature to be 300 K, $\Delta T_M \gtrsim 120 \text{ K}$ would change the antiferromagnetic order since the Néel temperature for Mn₃Sn is approximately 420 K. If we consider $d_{\text{sub}} = 2 \mu\text{m}$, then $\Delta T_M < 120 \text{ K}$ for $J_c < 9.4 \times 10^7 \text{ A}/\text{cm}^2$. This limits the use

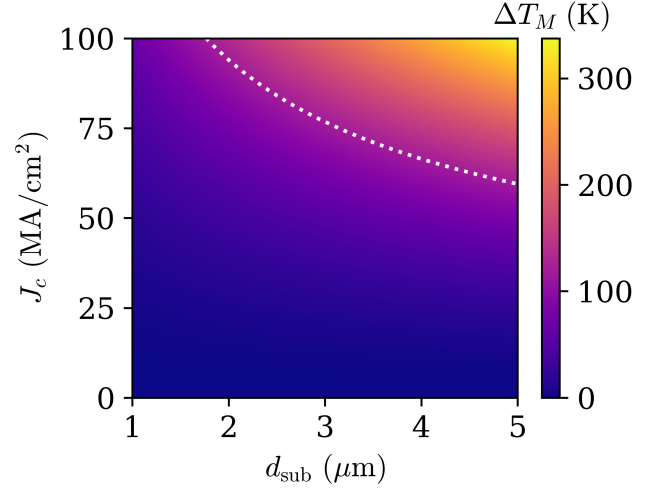


FIG. 12. Maximum possible rise in the junction temperature, ΔT_M , for different substrate thickness, d_{sub} , and input charge current density, J_c . ΔT_M increases with both d_{sub} and J_c , as expected. The dotted white line corresponds to $\Delta T_M = 120 \text{ K}$, which is the maximum temperature rise before the antiferromagnetic order in Mn₃Sn changes.

of a 4 nm thick Mn₃Sn film as a signal generator to about 33 GHz. On the other hand, for $d_{\text{sub}} = 5 \mu\text{m}$, the charge current density is limited to $J_c < 6 \times 10^7 \text{ A}/\text{cm}^2$, which limits the frequency of the signal source to about 21 GHz. The white dotted line overlaid on Fig. 12 represents this upper limit for the charge current for different substrate thicknesses. A thinner substrate, or the metallic heat sources with smaller area of cross-section could help lower the maximum temperature rise.

The time to reach ΔT_M , on the other hand, depends on τ . For a constant input current, $\Delta T_j(t)$ reaches to approximately 95% of ΔT_M in $t = 3\tau$. If we consider $d_{\text{sub}} = 1 \mu\text{m}$, then $\tau = 33.7 \text{ ns}$, and the time to reach 95% of the steady-state temperature is approximately 100 ns. Consequently, input currents larger than $J_c = 1.3 \times 10^8 \text{ A}/\text{cm}^2$ could be safely applied, if the duration of the pulse is of the order of few 10's of ps. Figure 13 shows the non quasi-static response of the rise in junction temperature, $\Delta T_j(t)$, as a function of time for current pulses of duration $t_{\text{pw}} = 100 \text{ ps}$. It can be observed that even for charge current density as large as $J_c = 3 \times 10^8 \text{ A}/\text{cm}^2$, the temperature rise is less than 24 K. Therefore, such large currents could be used during the switching operation, if required. Similar behavior is expected for other values of $t_{\text{pw}} \ll \tau$. A drawback of the high value of τ , due to large d_{sub} , is the slow removal of heat from the system, resulting in a slow decrease of temperature, as shown in Fig. 13. A thinner substrate or a substrate with lower thermal capacitance is preferred to reduce the time for heat to flow from the source to the sink, decreasing τ .

The aforementioned analysis does not consider the temperature dependence of the material parameters (electrical and thermal) of the AFM, the HM, or the substrate. In general, the material properties of the AFM, such as the uniaxial

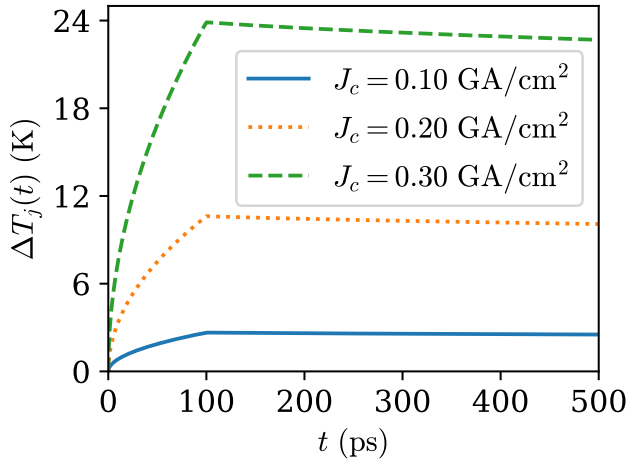


FIG. 13. Temperature rise of HM-Mn₃Sn bilayer due to Joule heating associated with the charge current pulse of different amplitudes, as indicated in the legend, and 100 ps duration. For $J_c = 3 \times 10^8$ A/cm², the temperature rise of the junction is approximately 24 K. On the other hand, for $J_c = 1 \times 10^8$ A/cm² and $J_c = 2 \times 10^8$ A/cm² the maximum temperature rise is approximately 2.7 K and 10.6 K, respectively. Once the input current pulse is turned off, the temperature begins to recover to the ambient temperature; however, the recovery is slow due to the large time constant of heat flow associated with the substrate.

anisotropy constant, could decrease with an increase in temperature due to Joule heating.¹⁸ Therefore, if the input current is slowly increased from zero to a higher value, the stationary steady-state solutions could be different from those given by Eq. (12) while the onset of dynamics could occur at an input current lower than that predicted by Eq. (13). The oscillation frequency at an input current (Eq. (14)), on the other hand, could increase owing to the lower threshold current as well as Joule heating induced lower saturation magnetization. Consequently, the order parameter could be switched at a faster rate using a current pulse of smaller duration since $J_s t_{pw}$ (Eq. (15)) would decrease. However, an exact value of the threshold current, stationary state, oscillation frequency, or minimum pulsewidth required to switch between two states as a function of the input current would depend on the relative change in the antiferromagnetic material parameters with temperature.

Non-zero temperature leads to random fluctuation of the AFM spins, and as a result the order parameter would exhibit a distribution around the equilibrium states in the six degenerate energy wells. When acted upon by external spin current the order parameter would exhibit stochastic dynamics—each stationary steady-state below the threshold current would show a distribution around a mean value, the oscillation frequency would exhibit a non-zero linewidth, and $J_s t_{pw}$ would show thermal noise-induced randomness. The effect of thermal fluctuations would be more prominent below and near threshold current while its effect on the dynamics would be weak for large values of input currents. Similar to ferromagnets, thermal noise in AFMs could be modeled as three random Gaussian fields, one for each sublattice, with zero mean

and standard deviation equal to one.⁵⁸ In our modeling approach, this field would be added to Eq. (8), and the total field would consist of those due to exchange interaction, DM interaction, uniaxial anisotropy, external field, and thermal noise. The goal of our work, however, was to understand the deterministic dynamics in monodomain Mn₃Sn, and therefore the effect of thermal noise is not considered here.

VII. CONCLUSION AND OUTLOOK

In this work, we investigated the SOT-driven oscillation and switching dynamics in six-fold magnetic anisotropy degenerate single-domain Mn₃Sn thin films. The spin polarization associated with the SOT was assumed perpendicular to the Kagome plane. Numerical simulations of the SOT-driven dynamics in the DC regime reveal that the frequency of oscillation of the order parameter in Mn₃Sn could be tuned from 100's of MHz to 100's of GHz by increasing the input spin current density. Analytic models of frequency versus input spin current density presented here for the first time show an excellent agreement with the numerical results, obtained by solving the classical coupled LLG equations of motion for the sublattice vectors of Mn₃Sn. In addition to the oscillatory dynamics, switching of the order parameter between the six energy minima could also be accomplished by utilizing pulsed input spin current. In this case, the switching of the order parameter can be controlled by tweaking the amplitude and the pulse width of the input spin current. To provide a physical insight into the physics and functionality of Mn₃Sn in the pulsed-SOT regime, we developed analytic models of the final state that the order parameter settles into as a function of the spin charge density and revealed excellent match with numerical results. Motivated by recent experimental advances in electrical detection of the magnetic state of Mn₃Sn, we discussed AHE and TMR as possible schemes to detect the state of the AFM in a microelectronics-compatible manner. We showed that AHE voltage signals could be in the range of $\sim \mu$ V, while the TMR voltage signals could be around 7–9 mV with a further possibility of increasing this voltage range for higher RA product values. Finally, we evaluated the temperature rise as a function of the input current pulse. Our results showed that the maximum temperature rise for MgO substrate of thickness $d_{sub} = 1 \mu$ m is less than 24 K for current pulses with $t_{pw} \leq 100$ ps and $J_c \leq 3 \times 10^8$ A/cm². On the other hand, in the DC mode, the maximum temperature rise is found to be 120 K for $J_c = 1.3 \times 10^8$ A/cm², thereby limiting the application of Mn₃Sn as a coherent signal generator for frequencies up to 45 GHz. In this work, we considered thin films with thicknesses less than 10 nm. Typically, such films show two-fold degeneracy, instead of the six-fold, owing to epitaxial strain. This will be addressed in our future work.

SUPPLEMENTARY MATERIAL

See supplementary material for the perturbative analysis of the ground state.

ACKNOWLEDGMENTS

This research was primarily supported by the NSF through the University of Illinois at Urbana-Champaign Materials Research Science and Engineering Center DMR-1720633.

DATA AVAILABILITY STATEMENT

The data that support the findings of this study are available from the corresponding author upon reasonable request.

- ¹E. Gomonay and V. Loktev, "Spintronics of antiferromagnetic systems," *Low Temperature Physics* **40**, 17–35 (2014).
- ²V. Baltz, A. Manchon, M. Tsoi, T. Moriyama, T. Ono, and Y. Tserkovnyak, "Antiferromagnetic spintronics," *Reviews of Modern Physics* **90**, 015005 (2018).
- ³M. B. Jungfleisch, W. Zhang, and A. Hoffmann, "Perspectives of antiferromagnetic spintronics," *Physics Letters A* **382**, 865–871 (2018).
- ⁴T. Jungwirth, X. Marti, P. Wadley, and J. Wunderlich, "Antiferromagnetic spintronics," *Nature Nanotechnology* **11**, 231 (2016).
- ⁵R. Cheng, D. Xiao, and A. Brataas, "Terahertz antiferromagnetic spin Hall nano-oscillator," *Physical Review Letters* **116**, 207603 (2016).
- ⁶R. Khymyn, I. Lisenkov, V. Tiberkevich, B. A. Ivanov, and A. Slavin, "Antiferromagnetic THz-frequency Josephson-like oscillator driven by spin current," *Scientific Reports* **7**, 43705 (2017).
- ⁷O. Gomonay, V. Baltz, A. Brataas, and Y. Tserkovnyak, "Antiferromagnetic spin textures and dynamics," *Nature Physics* **14**, 213–216 (2018).
- ⁸S. A. Siddiqui, J. Sklenar, K. Kang, M. J. Gilbert, A. Schleife, N. Mason, and A. Hoffmann, "Metallic antiferromagnets," *Journal of Applied Physics* **128**, 040904 (2020).
- ⁹S. M. Rezende, A. Azevedo, and R. L. Rodríguez-Suárez, "Introduction to antiferromagnetic magnons," *Journal of Applied Physics* **126**, 151101 (2019).
- ¹⁰O. R. Sulymenko, O. V. Prokopenko, V. S. Tiberkevich, A. N. Slavin, B. A. Ivanov, and R. S. Khymyn, "Terahertz-frequency spin Hall auto-oscillator based on a canted antiferromagnet," *Physical Review Applied* **8**, 064007 (2017).
- ¹¹O. Gomonay, T. Jungwirth, and J. Sinova, "Narrow-band tunable terahertz detector in antiferromagnets via staggered-field and antidamping torques," *Physical Review B* **98**, 104430 (2018).
- ¹²A. Parthasarathy, E. Cogulu, A. D. Kent, and S. Rakheja, "Precessional spin-torque dynamics in biaxial antiferromagnets," *Physical Review B* **103**, 024450 (2021).
- ¹³D.-Y. Zhao, P.-B. He, and M.-Q. Cai, "Terahertz oscillation in a non-collinear antiferromagnet under spin-orbit torques," *Physical Review B* **104**, 214423 (2021).
- ¹⁴A. Shukla and S. Rakheja, "Spin-torque-driven terahertz auto-oscillations in noncollinear coplanar antiferromagnets," *Physical Review Applied* **17**, 034037 (2022).
- ¹⁵Y.-Q. Zhao, P.-B. He, and M.-Q. Cai, "Tunable range of terahertz oscillations triggered by the spin hall effect in a biaxial antiferromagnet," *Physical Review B* **106**, 134427 (2022).
- ¹⁶T. Kosub, M. Kopte, R. Hühne, P. Appel, B. Shields, P. Maletinsky, R. Hübner, M. O. Liedke, J. Fassbender, O. G. Schmidt, *et al.*, "Purely antiferromagnetic magnetoelectric random access memory," *Nature communications* **8**, 13985 (2017).
- ¹⁷K. Olejník, T. Seifert, Z. Kašpar, V. Novák, P. Wadley, R. P. Campion, M. Baumgartner, P. Gambardella, P. Němec, J. Wunderlich, *et al.*, "Terahertz electrical writing speed in an antiferromagnetic memory," *Science advances* **4**, eaar3566 (2018).
- ¹⁸J. Han, R. Cheng, L. Liu, H. Ohno, and S. Fukami, "Coherent antiferromagnetic spintronics," *Nature Materials* , 1–12 (2023).
- ¹⁹C. Hahn, G. De Loubens, V. V. Naletov, J. B. Youssef, O. Klein, and M. Viret, "Conduction of spin currents through insulating antiferromagnetic oxides," *Europhysics Letters* **108**, 57005 (2014).
- ²⁰S. Rezende, R. Rodríguez-Suárez, and A. Azevedo, "Diffusive magnonic spin transport in antiferromagnetic insulators," *Physical Review B* **93**, 054412 (2016).
- ²¹S. M. Wu, W. Zhang, K. Amit, P. Borisov, J. E. Pearson, J. S. Jiang, D. Ledornerman, A. Hoffmann, and A. Bhattacharya, "Antiferromagnetic spin seebeck effect," *Physical review letters* **116**, 097204 (2016).
- ²²A. Mahmood, W. Echtenkamp, M. Street, J.-L. Wang, S. Cao, T. Komesu, P. A. Dowben, P. Buragohain, H. Lu, A. Gruverman, *et al.*, "Voltage controlled néel vector rotation in zero magnetic field," *Nature communications* **12**, 1674 (2021).
- ²³J. Nogués and I. K. Schuller, "Exchange bias," *Journal of Magnetism and Magnetic Materials* **192**, 203–232 (1999).
- ²⁴W. Zhang and K. M. Krishnan, "Epitaxial exchange-bias systems: From fundamentals to future spin-orbitronics," *Materials Science and Engineering: R: Reports* **105**, 1–20 (2016).
- ²⁵W. Zhang, W. Han, S.-H. Yang, Y. Sun, Y. Zhang, B. Yan, and S. S. Parkin, "Giant facet-dependent spin-orbit torque and spin hall conductivity in the triangular antiferromagnet IrMn₃," *Science Advances* **2**, e1600759 (2016).
- ²⁶J. Kübler and C. Felser, "Non-collinear antiferromagnets and the anomalous hall effect," *Europhysics Letters* **108**, 67001 (2014).
- ²⁷Y. Zhang, Y. Sun, H. Yang, J. Železný, S. P. Parkin, C. Felser, and B. Yan, "Strong anisotropic anomalous hall effect and spin hall effect in the chiral antiferromagnetic compounds Mn₃X (X = Ge, Sn, Ga, Ir, Rh, and Pt)," *Physical Review B* **95**, 075128 (2017).
- ²⁸H. Iwaki, M. Kimata, T. Ikebuchi, Y. Kobayashi, K. Oda, Y. Shiota, T. Ono, and T. Moriyama, "Large anomalous Hall effect in L12-ordered antiferromagnetic Mn₃Ir thin films," *Applied Physics Letters* **116**, 022408 (2020).
- ²⁹J. Železný, Y. Zhang, C. Felser, and B. Yan, "Spin-polarized current in noncollinear antiferromagnets," *Physical review letters* **119**, 187204 (2017).
- ³⁰G. Q. Yan, S. Li, H. Lu, M. Huang, Y. Xiao, L. Wernert, J. A. Brock, E. E. Fullerton, H. Chen, H. Wang, *et al.*, "Quantum sensing and imaging of spin-orbit-torque-driven spin dynamics in the non-collinear antiferromagnet Mn₃Sn," *Advanced Materials* **34**, 2200327 (2022).
- ³¹X. Wang, H. Yan, X. Zhou, H. Chen, Z. Feng, P. Qin, Z. Meng, L. Liu, and Z. Liu, "Noncollinear Mn₃Sn for antiferromagnetic spintronics," *Materials Today Physics* , 100878 (2022).
- ³²X. Wang, M. T. Hossain, T. Thapaliya, D. Khadka, S. Lendinez, H. Chen, M. F. Doty, M. B. Jungfleisch, S. Huang, X. Fan, *et al.*, "Spin currents with unusual spin orientations in noncollinear weyl antiferromagnetic Mn₃Sn," *Physical Review Materials* **7**, 034404 (2023).
- ³³Y. Takeuchi, Y. Yamane, J.-Y. Yoon, R. Itoh, B. Jinnai, S. Kanai, J. Ieda, S. Fukami, and H. Ohno, "Chiral-spin rotation of non-collinear antiferromagnet by spin-orbit torque," *Nature Materials* **20**, 1364–1370 (2021).
- ³⁴B. Pal, B. K. Hazra, B. Göbel, J.-C. Jeon, A. K. Pandeya, A. Chakraborty, O. Busch, A. K. Srivastava, H. Deniz, J. M. Taylor, *et al.*, "Setting of the magnetic structure of chiral kagome antiferromagnets by a seeded spin-orbit torque," *Science Advances* **8**, eabo5930 (2022).
- ³⁵G. K. Krishnaswamy, G. Sala, B. Jacot, C.-H. Lambert, R. Schlitz, M. D. Rossell, P. Noël, and P. Gambardella, "Time-dependent multistate switching of topological antiferromagnetic order in Mn₃Sn," *Physical Review Applied* **18**, 024064 (2022).
- ³⁶X. Chen, T. Higo, K. Tanaka, T. Nomoto, H. Tsai, H. Idzuchi, M. Shiga, S. Sakamoto, R. Ando, H. Kosaki, *et al.*, "Octupole-driven magnetoresistance in an antiferromagnetic tunnel junction," *Nature* **613**, 490–495 (2023).
- ³⁷H. V. Gomonay, R. V. Kunitsyn, and V. M. Loktev, "Symmetry and the macroscopic dynamics of antiferromagnetic materials in the presence of spin-polarized current," *Physical Review B* **85**, 134446 (2012).
- ³⁸O. Gomonay and V. Loktev, "Using generalized Landau-Lifshitz equations to describe the dynamics of multi-sublattice antiferromagnets induced by spin-polarized current," *Low Temperature Physics* **41**, 698–704 (2015).
- ³⁹T. Chirac, J.-Y. Chauleau, P. Thibaudeau, O. Gomonay, and M. Viret, "Ultrafast antiferromagnetic switching in nio induced by spin transfer torques," *Physical Review B* **102**, 134415 (2020).
- ⁴⁰S. Tomiyoshi and Y. Yamaguchi, "Magnetic structure and weak ferromagnetism of Mn₃Sn studied by polarized neutron diffraction," *Journal of the Physical Society of Japan* **51**, 2478–2486 (1982).
- ⁴¹A. Markou, J. Taylor, A. Kalache, P. Werner, S. Parkin, and C. Felser, "Noncollinear antiferromagnetic Mn₃Sn films," *Physical Review Materials* **2**, 051001 (2018).

- ⁴²J. Liu and L. Balents, “Anomalous hall effect and topological defects in antiferromagnetic weyl semimetals: Mn₃Sn/Ge,” *Physical Review Letters* **119**, 087202 (2017).
- ⁴³X. Li, S. Jiang, Q. Meng, H. Zuo, Z. Zhu, L. Balents, and K. Behnia, “Free energy of twisting spins in Mn₃Sn,” *Physical Review B* **106**, L020402 (2022).
- ⁴⁴Y. Yamane, O. Gomonay, and J. Sinova, “Dynamics of noncollinear antiferromagnetic textures driven by spin current injection,” *Physical Review B* **100**, 054415 (2019).
- ⁴⁵V. Puliafito, R. Khymyn, M. Carpentieri, B. Azzerboni, V. Tiberkevich, A. Slavin, and G. Finocchio, “Micromagnetic modeling of terahertz oscillations in an antiferromagnetic material driven by the spin hall effect,” *Physical Review B* **99**, 024405 (2019).
- ⁴⁶T. Higo, K. Kondou, T. Nomoto, M. Shiga, S. Sakamoto, X. Chen, D. Nishio-Hamane, R. Arita, Y. Otani, S. Miwa, *et al.*, “Perpendicular full switching of chiral antiferromagnetic order by current,” *Nature* **607**, 474–479 (2022).
- ⁴⁷Y. Sato, Y. Takeuchi, Y. Yamane, J.-Y. Yoon, S. Kanai, J. Ieda, H. Ohno, and S. Fukami, “Thermal stability of non-collinear antiferromagnetic mn₃sn nanodot,” *Applied Physics Letters* **122** (2023).
- ⁴⁸H. Tsai, T. Higo, K. Kondou, T. Nomoto, A. Sakai, A. Kobayashi, T. Nakano, K. Yakushiji, R. Arita, S. Miwa, *et al.*, “Electrical manipulation of a topological antiferromagnetic state,” *Nature* **580**, 608–613 (2020).
- ⁴⁹J. Hirst, U. Atxitia, S. Ruta, J. Jackson, L. Petit, and T. Ostler, “Multiscale modelling of the antiferromagnet Mn₂Au: From ab-initio to micromagnetics,” arXiv preprint arXiv:2206.08625 (2022).
- ⁵⁰T. Nagamiya, S. Tomiyoshi, and Y. Yamaguchi, “Triangular spin configuration and weak ferromagnetism of mn₃sn and mn₃ge,” *Solid State Communications* **42**, 385–388 (1982).
- ⁵¹P. Zhang, *Current-induced Dynamics of Easy-Plane Antiferromagnets*, Ph.D. thesis, Massachusetts Institute of Technology (2023).
- ⁵²I. D. Mayergoyz, G. Bertotti, and C. Serpico, *Nonlinear magnetization dynamics in nanosystems* (Elsevier, 2009).
- ⁵³H. Tsai, T. Higo, K. Kondou, S. Sakamoto, A. Kobayashi, T. Matsuo, S. Miwa, Y. Otani, and S. Nakatsuji, “Large hall signal due to electrical switching of an antiferromagnetic weyl semimetal state,” *Small Science* **1**, 2000025 (2021).
- ⁵⁴N. H. Sung, F. Ronning, J. D. Thompson, and E. D. Bauer, “Magnetic phase dependence of the anomalous hall effect in Mn₃Sn single crystals,” *Applied Physics Letters* **112**, 132406 (2018).
- ⁵⁵J. Dong, X. Li, G. Gurung, M. Zhu, P. Zhang, F. Zheng, E. Y. Tsymbal, and J. Zhang, “Tunneling magnetoresistance in noncollinear antiferromagnetic tunnel junctions,” *Physical Review Letters* **128**, 197201 (2022).
- ⁵⁶R. L. Coffie, *Characterizing and suppressing DC-to-RF dispersion in aluminum gallium nitride/gallium nitride high electron mobility transistors* (University of California, Santa Barbara, 2003).
- ⁵⁷M. Meinert, D. Graulich, and T. Matalla-Wagner, “Electrical switching of antiferromagnetic Mn₂Au and the role of thermal activation,” *Physical Review Applied* **9**, 064040 (2018).
- ⁵⁸D. Go, M. Sallermann, F. R. Lux, S. Blügel, O. Gomonay, and Y. Mokrousov, “Noncollinear spin current for switching of chiral magnetic textures,” *Physical Review Letters* **129**, 097204 (2022).